

---

This item was submitted to [Loughborough's Research Repository](#) by the author.  
Items in Figshare are protected by copyright, with all rights reserved, unless otherwise indicated.

## **Influence of weld thermal cycle and post weld heat treatment on the microstructure of MarBN steel**

PLEASE CITE THE PUBLISHED VERSION

<https://doi.org/10.1016/j.ijpvp.2019.05.010>

PUBLISHER

© the Authors. Published by Elsevier BV

VERSION

VoR (Version of Record)

PUBLISHER STATEMENT

This work is made available according to the conditions of the Creative Commons Attribution 4.0 International (CC BY 4.0) licence. Full details of this licence are available at: <http://creativecommons.org/licenses/by/4.0/>

LICENCE

CC BY 4.0

REPOSITORY RECORD

Guo, J., X. Xu, Mark Jepson, and Rachel Thomson. 2019. "Influence of Weld Thermal Cycle and Post Weld Heat Treatment on the Microstructure of Marbn Steel". figshare. <https://hdl.handle.net/2134/38046>.



# Influence of weld thermal cycle and post weld heat treatment on the microstructure of MarBN steel

J. Guo<sup>1</sup>, X. Xu<sup>1</sup>, Mark A.E. Jepson\*, R.C. Thomson

Department of Materials, Loughborough University, Epinal Way, Loughborough, Leicestershire, LE11 3TU, UK



## ARTICLE INFO

**Keywords:**  
MarBN steel  
HAZ  
Microstructure  
Precipitation

## ABSTRACT

Martensitic steels strengthened by Boron and Nitrogen additions (MarBN) were developed for high temperature/high stress service in power plant for periods of many years and are being considered as a promising candidate for the replacement of the more conventional Grade 91/92 steels. In the present study, extensive microstructural observation of physically simulated Heat Affected Zone (HAZ) MarBN material has been carried out after dilatometry simulations to link the variation in microstructure with weld thermal cycles. The microstructure in the MarBN HAZ has been observed to vary from a refined equiaxed morphology to a duplex microstructure consisting of refined grains distributed on the pre-existing Prior Austenite Grain Boundaries (PAGBs) as the peak temperature of the weld thermal cycle decreases. The temperature range corresponding to the formation of the duplex grain structure coincides with the temperature regime for the dissolution of the pre-existing  $M_{23}C_6$  carbides. An even distribution of the  $M_{23}C_6$  carbides within the martensitic substructure was also observed after Post Weld Heat Treatment (PWHT), which is beneficial for the creep performance of the weld HAZ. The MX precipitates are more resistant to thermal exposure and are not completely dissolved until the peak temperature reaches 1573 K (1300 °C). The Nb-rich MX precipitates are the predominant type observed both after weld simulations and PWHT. The hardness between the materials experienced with the thermal cycles with different peak temperature does not significantly vary after PWHT conducted in an appropriate condition, which is likely to mitigate an unfavourable stress condition in the localised area within the HAZ.

## 1. Introduction

MarBN steel, based around the general composition of 9Cr-3W-3Co-VNbN, is a recently developed material and is a promising candidate for the replacement of the more conventional 9–12% Cr steels for the applications of hot section components including tubes, pipes and headers within thermal powerplant. Compared to the more conventional materials, including the Grade 91 and Grade 92 steels, MarBN steel has demonstrated a superior creep strength and improved oxidation resistance [1–3]. This is achieved by an increased content of solid solution elements in combination with a balanced content of minor elements to provide an additional precipitation strengthening effect [4]. The addition of B at an increased level in combination with a balanced content of N further enhances the performance of MarBN steel upon long-term creep exposure. This is due to an effectively stabilised precipitate structure of  $M_{23}C_6$  carbides, as a result of the addition of B, and a well-dispersed distribution of nano-scale MX carbonitride particles formed upon the addition of N at an optimised level [3,4].

The manufacturing of components made from MarBN steel commonly involves welding processes to achieve appropriate joints within the system. Although components made from MarBN steels have been successively fabricated using a variety of welding processes [2,5], weld joints commonly introduce relatively vulnerable areas within structures. Similar to other 9–12% Cr steels, the welds fabricated with MarBN steel as the parent metal demonstrate a deteriorated creep resistance as compared to the bulk material in a high temperature and low stress regime [6,7]. Within other 9–12%Cr steels, creep failure in these welds typically occurs in the region close to the boundary between the heat affected zone (HAZ) and the parent metal [8,9], which is termed as ‘Type IV’ failure [10].

Extensive research activities have therefore been conducted on 9–12% Cr steel welds to understand the link between Type IV failure and local microstructural differences within the HAZ. The presence of Type IV failure was initially linked to a particularly soft region formed during weld thermal cycles with an inter-critical peak temperature [11]. However, experimental observations from other existing studies

\* Corresponding author.

E-mail address: [m.a.e.jepson@lboro.ac.uk](mailto:m.a.e.jepson@lboro.ac.uk) (M.A.E. Jepson).

<sup>1</sup> J. Guo and X. Xu contributed equally to this work so should be considered joint first authors.

are not in full agreement with this, since the failure locations of the welds showing Type IV failure behaviour are not completely aligned with the softest region in the HAZ [8,12]. The HAZ region with a refined microstructure has been linked to the rupture location through Type IV failure in other existing studies [13]. However, there have been experimental observations showing that the failure does not always occur in the region with the most refined microstructure [14]. Type IV failure has also been linked with the region showing a microstructure that does not have an optimised creep resistance [15–17]. However, due to a lack of systematic description of the microstructural distribution in the HAZ of complicated multi-pass welds, the critical regions corresponding to the location of Type IV failure has not yet been clearly indicated in the HAZ of the 9–12% Cr steel welds, including those in MarBN-type steels.

The microstructure in the HAZ is controlled by the local thermal gradient imparted by the welding process. Simplified models have been established in previous work to describe the microstructure in the HAZ of low alloy ferritic/bainitic steels [18,19]. Typically, the HAZ has been divided into several regions relating to the local peak temperature reached during the welding process. The microstructure in the HAZ is conventionally divided into four regions as follows: Coarse Grain (CG), Fine Grain (FG), Inter-Critical (IC) and Over-Tempered (OT) regions [18,19]. However, the existing definition of the HAZ do not seem satisfactory when defining the critical regions that are susceptible to creep damage in the HAZ of welds within 9–12 wt % Cr steel [20,21]. This is because the existing definition of the HAZ currently lacks a systematic description of key microstructural factors that are linked with the formation of creep damage. For instance, grain size can play a major role in controlling creep resistance where a larger grain size increases the creep resistance [22]. However, the distribution and quantity of  $M_{23}C_6$  carbides and fine MX-type carbonitrides in the martensitic matrix may also significantly affect the stability of a variety of boundaries under creep exposure [4,23,24].

In recent work on a single-pass weld fabricated within a parent metal of Grade 92 steel, the microstructure in the HAZ was systematically studied to link the microstructures produced to the thermal history in the HAZ [21]. The zones within the microstructure of the HAZ were therefore classified based on the gradient of peak temperature as: Completely Transformed (CT), Partially Transformed (PT) and Over-Tempered (OT) regions [21]. The PT-HAZ regions that are exposed to a weld thermal cycle with an inter-critical peak temperature were further indicated as the region most susceptible to creep damage [25]. In other recent work that compared the microstructure in the HAZ between the welds fabricated on the MarBN and Grade 92 parent metals, a similar microstructural gradient was observed between both welds except that the region showing a fine-grained structure was absent, in combination with a more refined precipitate structure in the weld on a MarBN parent metal [7]. However, as a *post-mortem* analysis focused on the final resultant microstructure after Post Weld Heat Treatment (PWHT), this work has not explicitly established the link between microstructure and heat input during welding. In addition, there is a lack of systematic assessment on the formation and distribution of secondary precipitate particles both during welding and PWHT, which is indeed of significant importance for the prediction of creep performance of weld joints.

In the present study, the properties and microstructures of simulated HAZ structures within MarBN steels produced using dilatometer-based simulations have been systematically examined to provide an explicit description of the microstructural gradient within the as-welded microstructure as a function of local peak temperature ( $T_p$ ) experienced. The influence of PWHT on the physically simulated as-welded microstructure has been further studied to thoroughly describe the resultant HAZ microstructure after PWHT. This further contributes to a more accurate identification of the critical HAZ regions and will assist in determining which of these may be particularly susceptible to creep damage.

**Table 1**

Chemical composition of the IBN1 parent metal (wt. %), balance is Fe.

C	Si	Mn	P	S	Cr	Mo	Ni	Al
0.1	0.45	0.54	0.012	0.004	8.74	0.05	0.14	0.007
B	Co	Cu	Nb	V	W	N		
0.012	3.02	0.04	0.06	0.21	2.53	0.018		

## 2. Experimental procedure

### 2.1. Materials and heat treatment

The investigation was conducted using a MarBN steel with the composition shown in Table 1, known as IBN1. The material was sectioned from an ingot in the as-cast condition and subsequently underwent a normalisation process at 1473 K (1200 °C) for 3 h and a tempering process at 1053 K (780 °C) for 3 h followed by air cooling.

Cylindrical specimens were then machined with a dimension of 5 mm in diameter and 10 mm in length. The thermal cycles applied to simulate the experienced HAZ temperatures during this study were based on the experimentally measured heat cycles and established simulations used in existing studies [21,26–28]. In this study, a heating rate of 100 K/s was applied in combination with a dwell time of 2 s at the required peak temperature ( $T_p$ ). Although it is accepted that heating rates may exceed this during real welding operations, the heating rate applied here is the maximum achievable in the equipment used. The cooling phase comprised three different stages with the rate ranging from 60 K/s to 8 K/s as shown in Fig. 1.

The transformation temperatures,  $Ac_1$  and  $Ac_3$  were measured from the dilation behaviour of the specimen as a function of temperature. These were measured within the dilatometer by determining the temperatures at which the dimensional change of the specimen started to deviate from a linear relationship with the variation of temperature as described in [21,29]. These transformation temperatures were determined using the weld simulation heating rate of 100 K/s to ensure that transformation temperatures were as expected for the high heating rates used in the applied weld simulation. Based on measurements from six individual specimens, the average  $Ac_1$  and  $Ac_3$  phase transformation temperatures were determined to be:  $1211 \pm 15$  K ( $938 \pm 15$  °C) and  $1342 \pm 15$  K ( $1069 \pm 15$  °C), respectively. Based on these transformation temperatures, four peak temperatures of primary interest were defined as listed in Table 2. In some parts of this study, an additional  $T_p$  of 1473 K (1200 °C) was applied in order to explore the limits of microstructural features or to provide an intermediate step between 1373 K (1100 °C) and 1573 K (1300 °C). After experiencing these

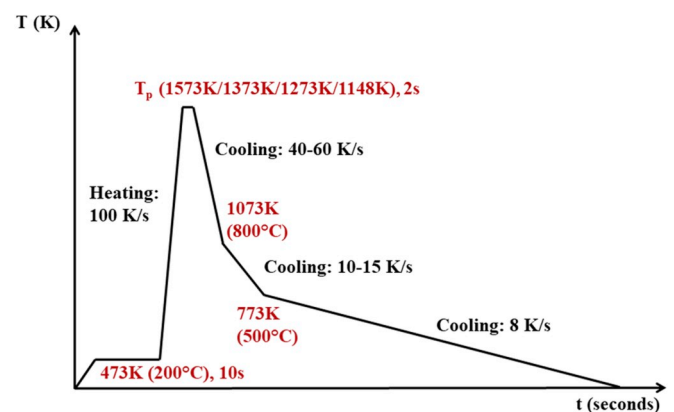
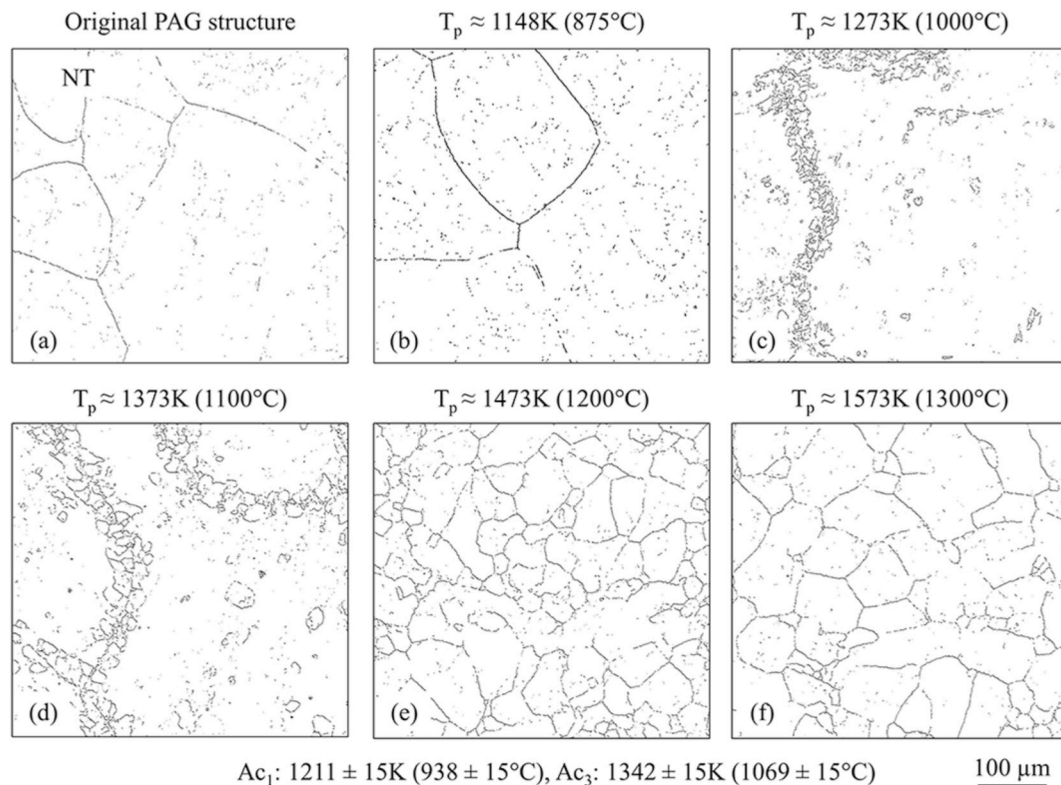


Fig. 1. A graph showing the details of the dilatometry heat cycle used for weld simulation.

**Table 2**

Temperatures used to simulate different HAZ regions within the dilatometer-based physical simulation of the weld thermal cycle.

Description of region	$T_p > A_{c3}$	$T_p > A_{c3}$	$A_{c1} < T_p < A_{c3}$	$T_p < A_{c1}$
Peak temperature, $T_p$	1573 K (1300 °C)	1373 K (1100 °C)	1273 K (1000 °C)	1148 K (875 °C)



**Fig. 2.** EBSD grain boundary maps showing only the high angle boundaries with 15–50° misorientation to reveal the characteristics of the PAG structure formed after weld simulations with various peak temperatures.

simulated heat cycles, half of the specimens were further heat treated at 1033 K (760 °C) for a duration of 2 h to simulate a Post Weld Heat Treatment procedure (PWHT).

## 2.2. Microstructural characterisation

Hardness testing was performed using a Struers® Durascan® 70 hardness testing system equipped with a Vickers indenter. The testing method used in the current research is consistent with the methodology of hardness testing as detailed in previous research conducted on a similar 9% Cr steel [30]. As a consequence, hardness indents were produced at an applied weight of 0.2 kg and a dwell of 10 s. A total of 100 indents were produced on each specimen with an inter-spacing distance of 0.1 mm to assess hardness with sufficient statistical significance.

Specimens for microstructural examination were prepared using conventional metallographic preparation methods finished by a chemo-mechanical polishing procedure using a 0.02 μm colloidal silica suspension.

An FEI Nova Nanolab 600 dual beam Focused Ion Beam (FIB)/Field Emission Gun Scanning Electron Microscope (FEG)-SEM was used for Electron Backscatter Diffraction (EBSD) analysis and ion beam induced Secondary Electron (SE) imaging. EBSD mapping was conducted at an accelerating voltage of 20 kV with a step size of 0.1 μm. These maps were used to study the grain microstructures with the location of high angle PAGBs highlighted by filtering the collected data to show just the boundaries with 15–50° misorientation. Ion beam induced SE micrographs were collected to reveal the location and sizes of secondary

phase particles with the ion beam operated at an accelerating voltage of 30 kV and a nominal beam current of 50 pA. In-situ XeF<sub>2</sub> gas etching was used to enhance the contrast differential between particles and the matrix. Precipitate particles were quantified using a grey scale segmentation methodology using ImageJ. Backscattered Electron (BSE) imaging was also conducted to characterise Laves phase particles after PWHT using the dual-beam FIB/FEG SEM. Due to the abundance of heavy elements, Laves phase particles were revealed as bright particles with a distinctively higher brightness than the matrix [31].

Chemical and crystallographic analyses of secondary precipitate particles were carried out using transmission electron microscopy (TEM) on membrane specimens prepared using a carbon extraction replication technique [21,32]. Precipitate particles were chemically identified using Energy Dispersive X-ray spectroscopy (EDX) in an FEI Tecnai F20 TEM equipped with an Oxford Instruments X-Max 80<sup>N</sup> TLE EDX system.

## 3. Results

### 3.1. Grain structure as a function of peak temperature

**Fig. 2** shows EBSD maps of the prior austenite grain (PAG) boundaries from a range of different peak temperatures ( $T_p$ ).

Within the original, as-received parent material, a coarse PAG structure was present and also within the material after a simulated weld thermal cycle with  $T_p < A_{c1}$  (**Fig. 2** (a) and (b), respectively). Fine austenite grains started to form along the pre-existing PAGBs after

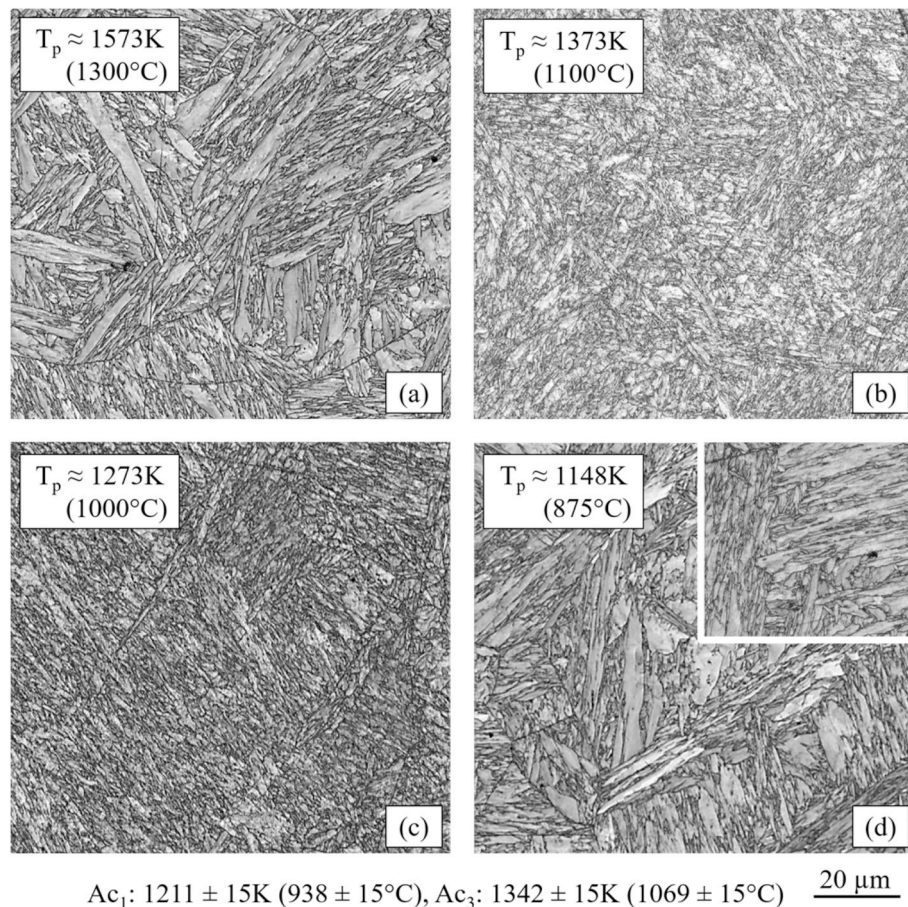


**Fig. 3.** EBSD Image Quality (IQ) maps showing the characteristics of martensitic substructures formed after weld simulations with various peak temperatures; a) 1573 K (1300 °C), b) 1373 K (1100 °C), c) 1273 K (1000 °C) and d) 1148 K (875 °C) with inset of the unaffected parent metal microstructure for comparison.

the heat treatment in which  $T_p$  reached  $\sim 1273$  K ( $\sim 1000$  °C), Fig. 2 (c). With increasing  $T_p$ , up to a  $T_p$  of  $\sim 1373$  K ( $\sim 1100$  °C), Fig. 2 (d), the newly-formed austenite grains were seen to have grown. When  $T_p$  reached an intermediate temperature of  $\sim 1473$  K ( $\sim 1200$  °C), a more homogeneous microstructure consisting of equiaxed austenite grains was present in the simulated HAZ microstructure, Fig. 2 (e). A greater number of equiaxed fine grains with a grain size of less than  $60 \mu m$  can be seen when  $T_p = \sim 1473$  K (1200 °C) (Fig. 2 (e)) than when  $T_p = \sim 1573$  K (1300 °C) (Fig. 2 (f)) that has a grain size of  $\sim 100 \mu m$ .

The martensitic substructure was further studied by EBSD analysis conducted at a step size of  $0.1 \mu m$ , Fig. 3.

The martensitic substructure in the region exposed to a  $T_p$  of  $\sim 1573$  K (1300 °C) (Fig. 3 (a)) is composed of lath-like martensitic blocks with a similar size to the region exposed to a  $T_p$  of  $\sim 1148$  K (875 °C) (Fig. 3 (d)). The martensitic structure in the fine austenite grains after experiencing a  $T_p$  of both  $\sim 1273$  K (1000 °C) and  $\sim 1373$  K (1100 °C) is much denser and composed of martensitic sub-grains less than  $10 \mu m$  in size, Fig. 3 (b) and (c) respectively. The martensitic substructure in the region exposed to a peak temperature of  $\sim 1148$  K (875 °C) shows no significant variation from the original substructure in the unaffected parent metal (see inset of Fig. 3 (d)).

### 3.2. Presence of $M_{23}C_6$ carbides after simulated weld thermal cycle and PWHT

The distribution of carbides within the matrix material after application of the simulated HAZ thermal cycle and PWHT were characterised using ion induced SE imaging, Fig. 4.

This technique has been proved to provide reliable information on the distribution of precipitate particles, particularly the  $M_{23}C_6$  carbides [21,33]. Here it can be seen that the number density of  $M_{23}C_6$  carbides varies after simulated thermal cycles with different peak temperatures. It was found that the carbides were completely dissolved when  $T_p \gg A_{c_3}$  at  $\sim 1573$  K (1300 °C). Carbides were only partially dissolved when  $T_p$  was between  $A_{c_1}$  and  $\sim 1573$  K (1300 °C). After PWHT, precipitates were formed and preferentially distributed on the martensitic substructure boundaries in the resulting microstructure of samples of all  $T_p$  temperatures.

The population of carbides after the simulated thermal cycles and PWHT were quantitatively measured as presented in Fig. 5 (a). The data shows that the distribution of grain boundary carbides significantly varies after experiencing different  $T_p$  within the weld thermal cycles. However, although the number density of carbides after a  $T_p$  of 1273 K (1000 °C) appears to be slightly lower, the standard deviation of the dataset suggests that the number of carbide particles after PWHT does not significantly vary, regardless of the  $T_p$  experienced within the simulated thermal cycles.

The size distribution of carbides in each of the simulated HAZ regions after PWHT was analysed and is summarised in Fig. 5 (b) with the peak carbide size in each specimen indicated by vertical lines. There is a higher number of carbides with a size of less than  $0.1 \mu m$  in the specimens which experienced  $T_p = \sim 1373$  K (1100 °C) and  $\sim 1273$  K (1000 °C) than the specimens which experienced a  $T_p = \sim 1148$  K (875 °C). This can be attributed to the presence of un-dissolved or partially dissolved precipitates after weld simulations that mitigated the formation of new precipitates during the applied PWHT stage.

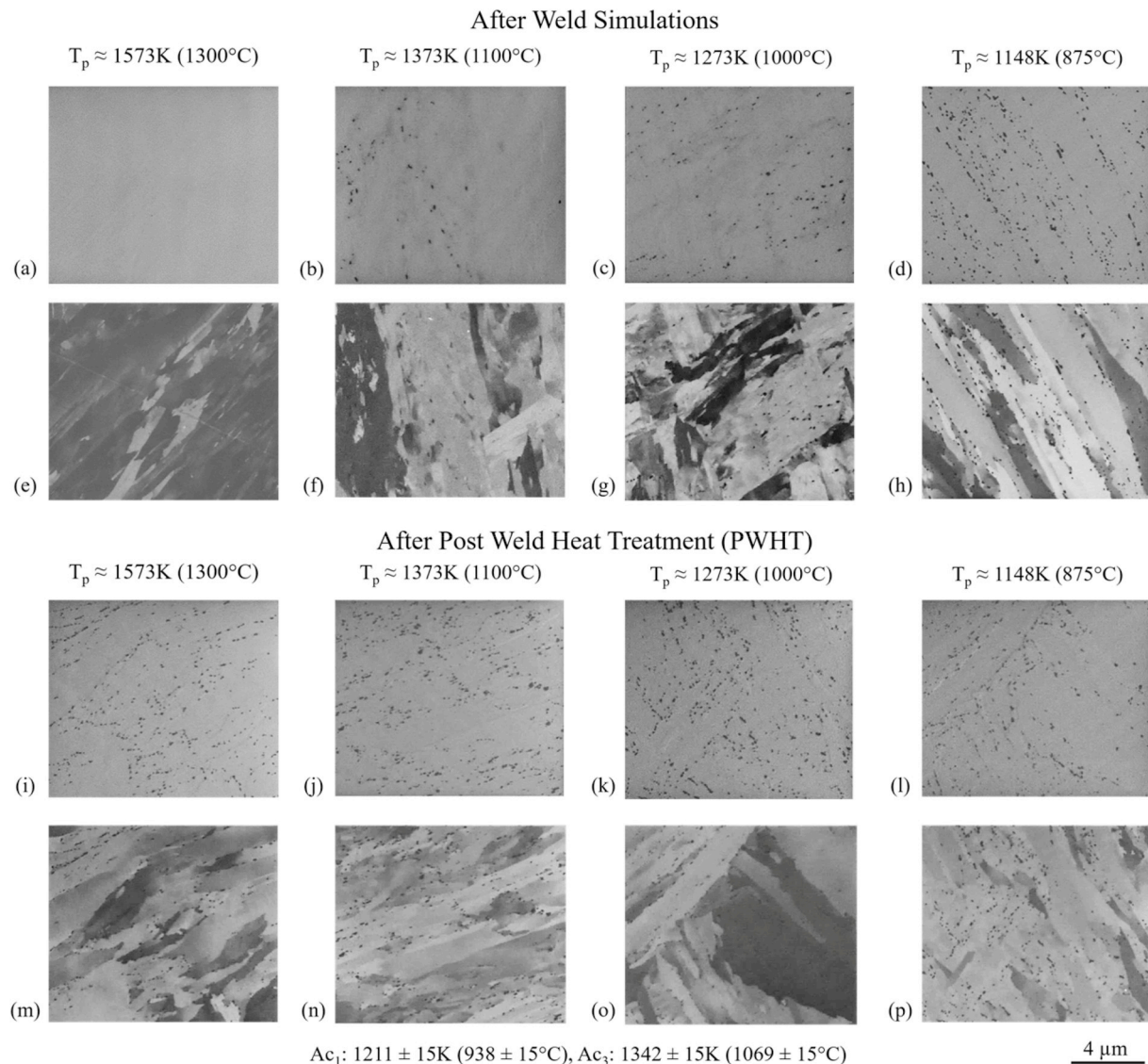


**Fig. 4.** Ion beam induced SE micrographs demonstrating the distribution of precipitates and sub-structure (a–h) after weld simulations with various peak temperatures and (i–p) after PWHT. Micrographs were collected using different ion doses from each specimen to visualise distribution of precipitates and characteristics of martensitic substructure.

### 3.3. Precipitation behaviour of fine MX-type carbonitrides

Fine precipitates in the microstructure were analysed using TEM. Fig. 6 demonstrates a BF-STEM micrograph showing the precipitates on a carbon extraction replica obtained after weld simulation with a peak temperature of  $\sim 1148\text{K}$  ( $875^\circ\text{C}$ ) and representative EDX spectra obtained from a selection of precipitate particles.

The precipitate particles within the extraction replica have a range of sizes and shapes as shown in Fig. 6 (a). The particles with a dark appearance are typically  $0.1\text{--}0.2\ \mu\text{m}$  in length with an elongated shape. These particles were identified to be enriched in Cr (Fig. 6 (b)) with a chemical composition close to that expected for  $M_{23}C_6$  carbides [24]. The size of these precipitates is also close to the particles observed by ion induced SE imaging as shown in Fig. 5. In addition, smaller particles measuring  $20\text{--}80\ \text{nm}$  in Feret diameter were also observed in the same specimen. These precipitates were identified to be enriched in Nb and V (Fig. 6 (c) and (d)) with a chemical composition close to that expected for MX carbonitrides [34].

The chemistry of the MX carbonitride particles in all specimens was

investigated using EDX after both weld simulations and PWHT with results summarised in Fig. 7.

The MX carbonitride was found to co-exist as either a Nb-rich or V-rich MX after a simulated HAZ thermal cycle with a  $T_p$  of  $\sim 1148\text{K}$  ( $875^\circ\text{C}$ ) (Fig. 7 (a)), whereas the Nb-rich MX particles became the more dominant type of precipitate after thermal cycles with a  $T_p$  of  $\sim 1273\text{K}$  ( $1000^\circ\text{C}$ ) and  $\sim 1373\text{K}$  ( $1100^\circ\text{C}$ ) (Fig. 7 (b) and 7 (c)). The pre-existing MX precipitates from the parent metal were completely dissolved after the thermal cycle with a  $T_p$  of  $\sim 1573\text{K}$  ( $1300^\circ\text{C}$ ) so are not included here. MX precipitates were also analysed after PWHT (Fig. 7 (d)–(g)). The chemistry of the MX precipitates does not significantly vary between samples of differing  $T_p$  after PWHT, with the majority being the Nb-rich type of carbonitride in combination with the V-rich precipitates at a minor level.

### 3.4. Precipitation of Laves phase during PWHT

The presence of Laves phase particles was not observed in the microstructure of the original parent metal nor after weld simulations.

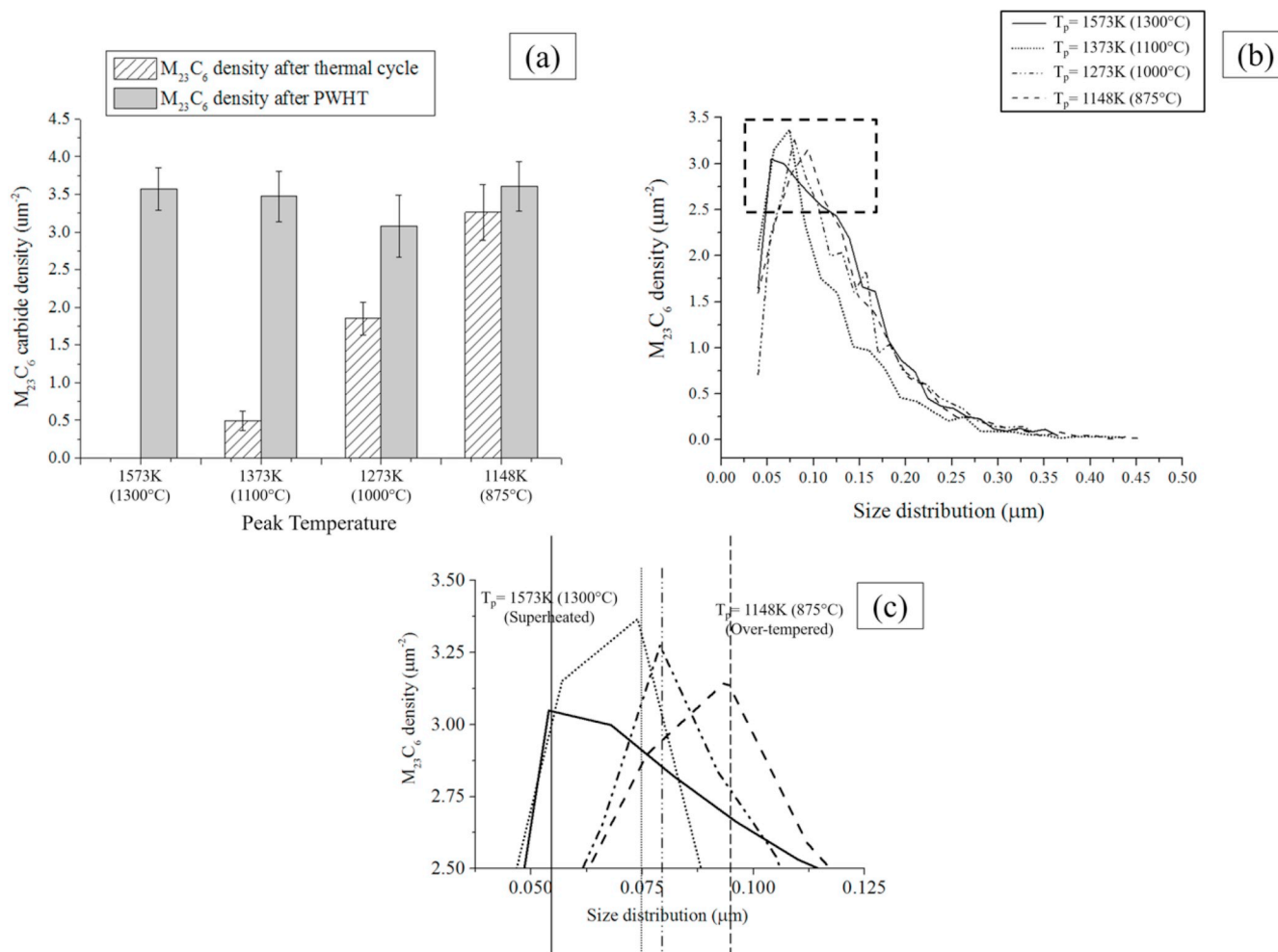


Fig. 5. Graphs demonstrating (a) number density, (b) size distribution and (c) expanded view of the area marked in (b) of the  $M_{23}C_6$  carbides after weld simulation and PWHT.

However, Laves phase was observed to form during the PWHT applied here (a temperature of 760 °C for 2 h). Fig. 8 is a collection of BSE micrographs showing the Laves phase in the microstructure after a combination of thermal cycles with different peak temperatures followed by the PWHT.

A lower number of Laves phase particles was observed after the thermal cycle with a  $T_p$  of ~1573 K (1300 °C) (Fig. 8 (a)) compared to the specimens which experienced lower peak temperatures. This can be linked with a relatively coarser substructure formed after weld simulation when  $T_p \gg A_{c3}$  (Fig. 3 (a)). However, the distribution of the Laves phase particles is also denser after a thermal cycle with a  $T_p$  of ~1148 K (875 °C), while the martensitic substructure in this specimen (Fig. 3 (d)) is similar to the microstructure formed after weld simulation with a  $T_p$  of ~1573 K (1300 °C) (Fig. 3 (a)). This is probably due to a less homogeneous distribution of the elements related with the formation of Laves phases (e.g. W) after weld simulations with a lower  $T_p$  at ~1148 K (875 °C).

### 3.5. The effect of PWHT on the HAZ hardness

The variation of hardness after the simulated weld thermal cycles and PWHT was further studied using Vickers hardness testing, Fig. 9.

The hardness of specimens exposed to weld thermal cycle simulations increased as  $T_p$  increased. This can be explained by the presence of

newly formed un-tempered martensite (Fig. 3) after weld simulations with a  $T_p$  of  $> A_{c1}$  [35]. This is also consistent with the observation from other 9% Cr steel welds that the microstructure with a higher hardness value is presented in the region close to the weld line [25]. The weld simulation with a  $T_p < A_{c1}$  at ~1148 K (875 °C) also leads to a slightly lower hardness than the original parent metal due to a tempering effect, which is also similar to the existing observations from Grade 92 steel [21,25].

The hardness in the specimens which experienced a weld simulation with a high  $T_p$  has been shown to significantly decrease during PWHT, whereas the hardness in the specimens which experienced a lower  $T_p$  did not significantly decrease after PWHT. This can be linked to a decrease in dislocation density and the precipitation of carbides during PWHT. It has been reported that the dislocation structure in newly-formed martensite is significantly altered during PWHT, which leads to a lower density network of dislocations and hence a lower hardness [36–38]. The decrease in hardness after PWHT can also be linked with the formation of the  $M_{23}C_6$  carbides and Laves phase particles. This is likely to reduce the concentrations of solid solution elements (e.g. Mo and W) in the matrix [39].

The significant decrease in hardness during PWHT of the specimens which experienced a higher  $T_p$ , also leads to a similar hardness level as the specimens which experienced a lower  $T_p$ . This suggests that the hardness gradient in the HAZ of a real weld is likely to be minimised after PWHT if conducted at appropriate temperatures.

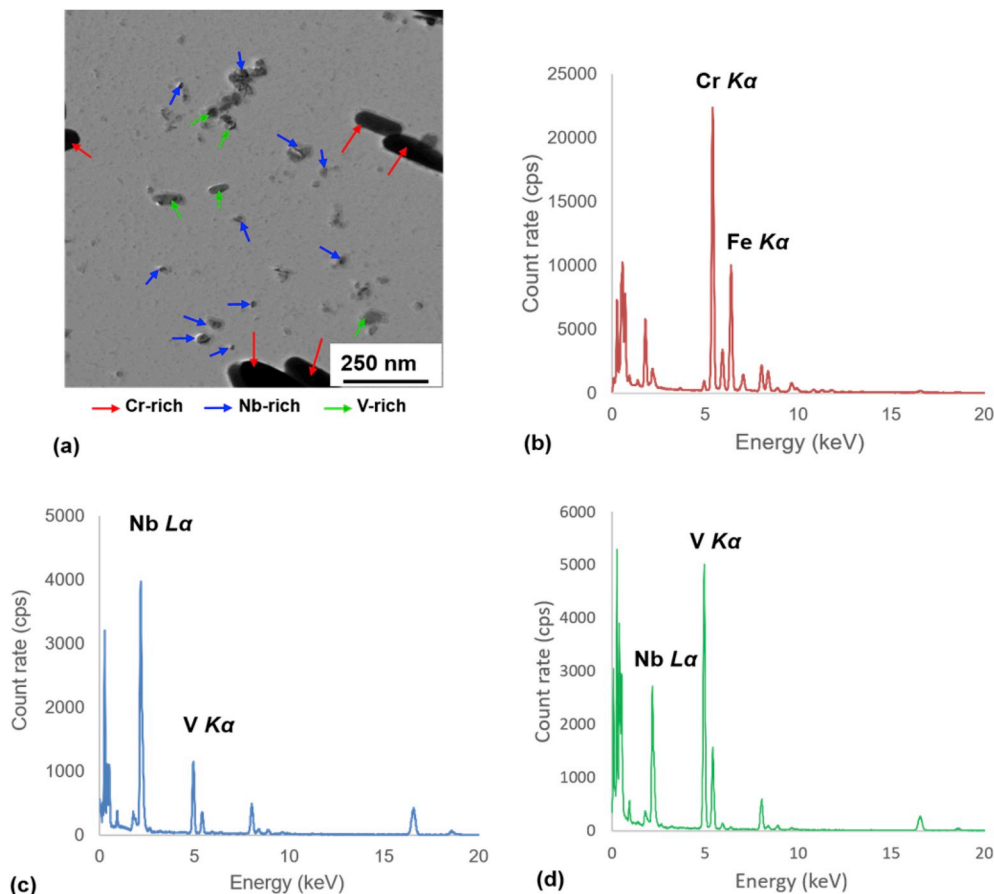


**Fig. 6.** (a) A BF-STEM micrograph showing precipitate particles on a carbon extraction replica obtained after weld simulation with a peak temperature of  $\sim 1148$  K (875 °C). The particles with different chemical compositions are indicated by arrows in different colours where red = Cr-rich, blue = Nb-rich and green = V-rich. The EDX spectra obtained from (b) Cr-rich, (c) Nb-rich and (d) V-rich precipitates are also included. (For interpretation of the references to colour in this figure legend, the reader is referred to the Web version of this article.)

#### 4. Discussion

The microstructure in the simulated weld specimens can be linked with the microstructure in the HAZ of real welds. It is known that the  $T_p$  of a weld thermal cycle is decreased with increasing distance from the weld fusion line within the HAZ of real welds, with the ultimate value of  $T_p$  close to 1500 °C in the area adjacent to the weld fusion line [40]. The  $T_p$  of the thermal cycles adopted for physical weld simulation in this study is also within the range determined by both Finite Element (FE) modelling [40,41] and experimental measurement [28]. Using these assumptions, it is therefore possible to summarise the variation in microstructure within the HAZ in MarBN steels as a function of approximate distance from the fusion line as shown in Fig. 10. On this diagram,  $M_{23}C_6$  particles are shown to be present on PAGBs of the structure only. It should be noted that, as well as these locations,  $M_{23}C_6$  particles are also observed to be present on lath boundaries within the martensite structure of the material as shown in Fig. 4.

An important observation is that the PAG structure varies significantly with the  $T_p$  experienced during the weld simulation. Starting from a PAG structure with a grain size of  $> 300 \mu\text{m}$  within the parent metal, refined PAGs start to form along the pre-existing PAG boundaries as  $T_p > A_{c1}$  ( $\sim 1200$  K (938 °C)). As  $T_p$  increased to a range between the  $A_{c1}$  and  $A_{c3}$ , the PAG structure is a mixture of refined PAGs along the pre-existing PAG boundaries from the parent metal. Such a PAG structure remains until  $T_p$  reaches  $\sim 1473$  K (1200 °C), above which the original PAG structure is completely replaced by an equiaxed PAG structure with a grain size of less than  $100 \mu\text{m}$ . This set of observations is consistent with previous work where the HAZ microstructure of B-containing steels was studied as a function of peak temperature [35] where a combination of diffusional and displacive reactions were suggested to be responsible for the appearance of newly formed, fine PAGs at the original PAGBs within a coarse-grained matrix, respectively, at

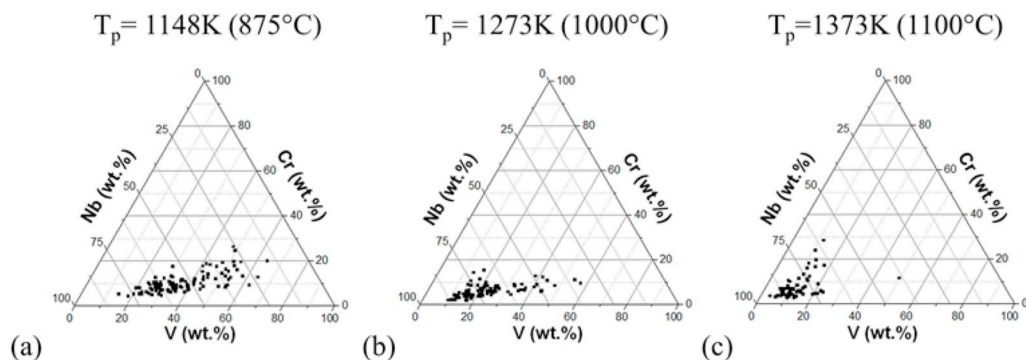
intermediate peak temperatures. To confirm the transformation process of the alloy studied here, further work would be required. The resultant PAG structure after welding is not significantly changed by PWHT.

Compared to previous observations from the HAZ of Grade 92 steel welds [25], the general trend of the PAG structure in the HAZ of IBN1 is similar. However, in the HAZ of Grade 92 steel, a duplex grain structure composed of refined PAGs on the pre-existing PAG boundaries and the residual domain of PAGs from the parent metal was only observed as  $T_p$  was in the inter-critical range between the  $A_{c1}$  and  $A_{c3}$  temperatures [21], whereas a similar PAG structure was also observed as  $T_p$  was  $> A_{c3}$  in IBN1. This may be attributed to a higher dissolution temperature of the  $M_{23}C_6$  carbides when compared to the Grade 92 steel. In Grade 92 steel, the  $M_{23}C_6$  carbides are completely dissolved as  $T_p$  reaches 1373 K (1100 °C), whereas the  $M_{23}C_6$  carbides in IBN1 are not completely dissolved until  $T_p \gg A_{c3}$ . The range of  $T_p$  during which the  $M_{23}C_6$  carbides are not dissolved corresponds to the  $T_p$  range at which a duplex PAG structure is observed. This indicates that, within IBN1, the growth of the newly-formed PAGs is effectively hindered due to the pinning effect from the un-dissolved  $M_{23}C_6$  carbide particles. This is also consistent with findings from previous work on MarBN steel welds [42].

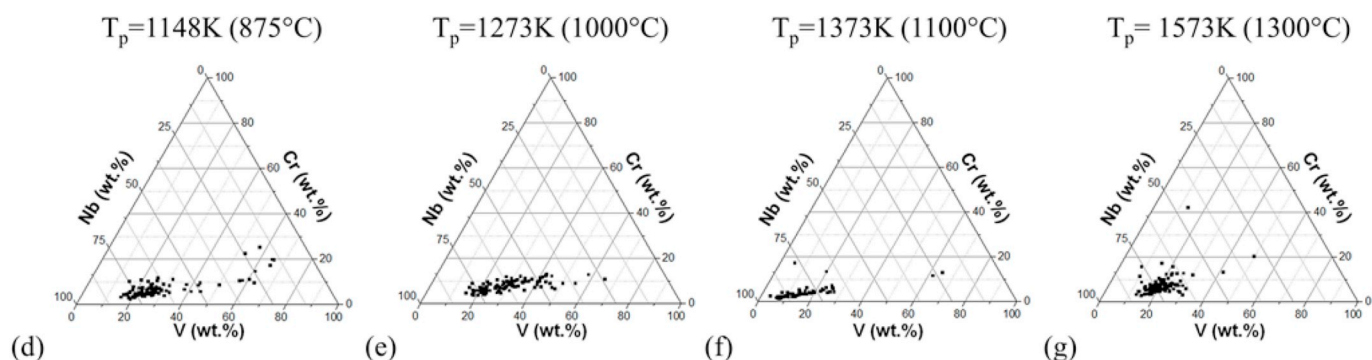
The martensitic substructure is relatively coarser after a weld simulation with a higher  $T_p$  of  $\sim 1573$  K (1300 °C), whereas the substructure is much more refined with a lower  $T_p$  of  $\sim 1373$  K (1100 °C) and  $\sim 1273$  K (1000 °C) (Fig. 3). This is attributed to a short time at high temperature and a high cooling rate experienced within the thermal cycles used for the weld simulation. Both the PAG structure and the martensitic substructure formed during weld simulations were preserved during PWHT, suggesting a good stability of the martensitic microstructure.

Secondary precipitates from the original parent metal are dissolved due to heat input during weld simulations. Thermodynamic calculation

## After Weld Simulations



## After PWHT



$$Ac_1: 1211 \pm 15\text{K} (938 \pm 15^\circ\text{C}), Ac_3: 1342 \pm 15\text{K} (1069 \pm 15^\circ\text{C})$$

Fig. 7. Ternary diagrams demonstrating the chemical composition of MX carbonitrides as a function of  $T_p$  after weld simulation and PWHT. The number of particles being analysed in each specimen is in the range of 80–100. No MX particles were present when  $T_p = 1573\text{K}$  ( $1300^\circ\text{C}$ ).

was adopted to understand the thermal stability of the major phases in IBN1 under an equilibrium state, Fig. 11.

The  $Ac_1$  and the  $Ac_3$  temperatures measured prior to weld simulations were found to be significantly higher than the predicted equilibrium transformation temperature. This is, however, consistent with observations from previous studies of 9% Cr steels in which a high heating rate was adopted for measurement [21,43]. The measured temperature for the dissolution of the  $M_{23}C_6$  carbides during weld simulation ( $\sim 1473\text{K}$  ( $1200^\circ\text{C}$ )) is also higher than the prediction from the equilibrium thermodynamic calculation. This is indeed related to the high heating rate applied during the thermal cycles and the short time period during which a high temperature was maintained. The dissolution of the pre-existing MX carbonitrides also shows similar behaviour. The Nb-rich MX precipitates are more stable than the  $M_{23}C_6$  carbides and the V-rich MX in the high temperature regime. These precipitates were not completely dissolved until the  $T_p$  of the weld simulation reached  $1573\text{K}$  ( $1300^\circ\text{C}$ ), whereas the relatively unstable V-rich MX precipitates appeared to be completely dissolved as  $T_p$  reached  $1373\text{K}$  ( $1100^\circ\text{C}$ ).

PWHT was conducted in the  $\alpha$ -Fe phase regime at a temperature of  $1033\text{K}$  ( $760^\circ\text{C}$ ). As a result, the martensitic microstructure formed during the weld simulation was not significantly altered during PWHT. The temperature of the PWHT was also within the range that  $M_{23}C_6$  carbides, the MX carbonitrides and Laves phase were predicted to be stable by the thermodynamic calculation. As a result, these phases were observed in the microstructure after PWHT. The  $M_{23}C_6$  carbides formed uniformly on the martensitic boundaries during PWHT. This suggests that the overall microstructure is effectively stabilised by the

precipitates distributed on substructure boundaries in all specimens regardless of  $T_p$  [4,20,44].

The specimen that experienced a  $T_p$  of  $\sim 1573\text{K}$  ( $1300^\circ\text{C}$ ) has the highest number of precipitate particles between  $0.1$  and  $0.2\ \mu\text{m}$  in size, whereas a higher number fraction of the  $M_{23}C_6$  carbides with a size of less than  $0.1\ \mu\text{m}$  was observed after weld simulation with a  $T_p$  of  $1373\text{K}$  ( $1100^\circ\text{C}$ ) and  $1273\text{K}$  ( $1000^\circ\text{C}$ ). Such a trend of distribution for the  $M_{23}C_6$  carbides was also observed in previous work on Grade 92 steel [21]. A higher fraction of smaller  $M_{23}C_6$  carbides can be attributed to an incomplete dissolution of pre-existing precipitates during the weld thermal cycle, which limits the carbide forming elements re-entering solution. In addition, the specimen which experienced a weld simulation with a  $T_p$  of  $1573\text{K}$  ( $1300^\circ\text{C}$ ) demonstrated an appropriate size distribution of the  $M_{23}C_6$  carbides for an optimum precipitation strengthening effect with a size range of  $0.1$ – $0.2\ \mu\text{m}$  [45]. This suggests that the overall microstructural stability is more enhanced by an even distribution of  $M_{23}C_6$  carbides in the specimen which experienced a  $T_p \gg Ac_3$ , corresponding to the regions more adjacent to the weld line in weld HAZ.

The presence of Laves phases was also observed after PWHT. Due to a relatively higher W content in MarBN steels, the tendency for Laves formation is higher than the conventional 9% Cr steels such as the Grade 91 and 92 steels. It is known that the fast growth of Laves phase is detrimental to the creep performance of 9% Cr steels as it rapidly consumes solid solution elements from the matrix [36,46]. Although *post-mortem* analyses after creep testing was not conducted in this study, a higher growth rate of Laves phase particles during creep exposure is expected due to a higher W content in the MarBN steel [47]. Therefore,

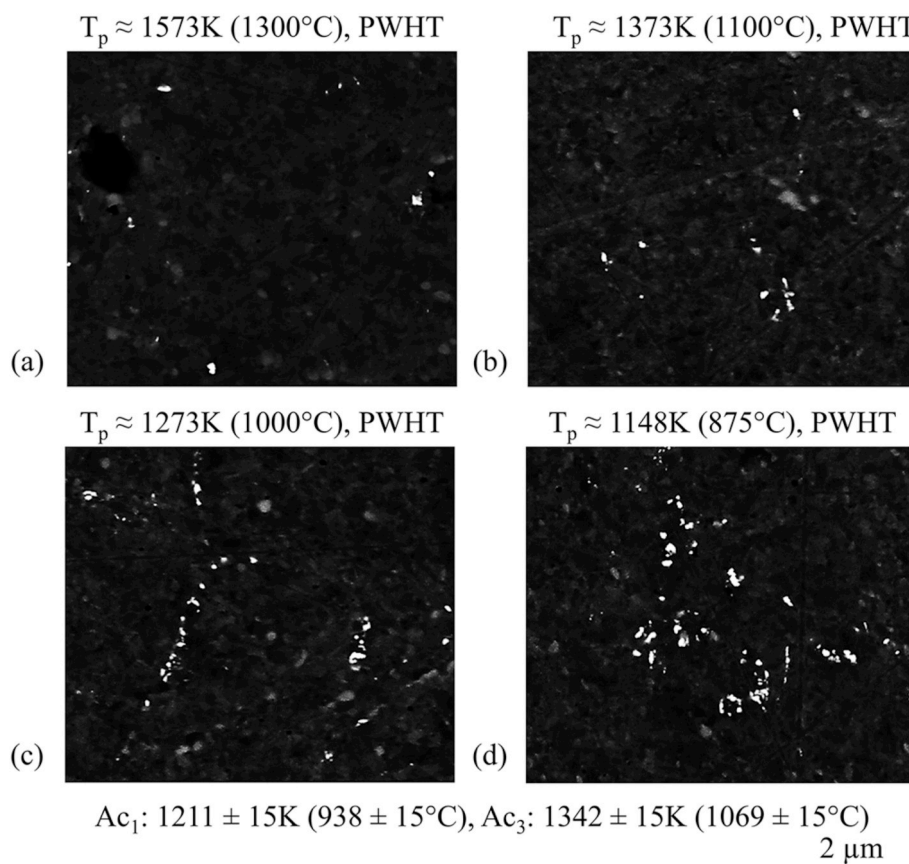


Fig. 8. Backscattered electron micrographs demonstrating the Laves phases formed after PWHT.

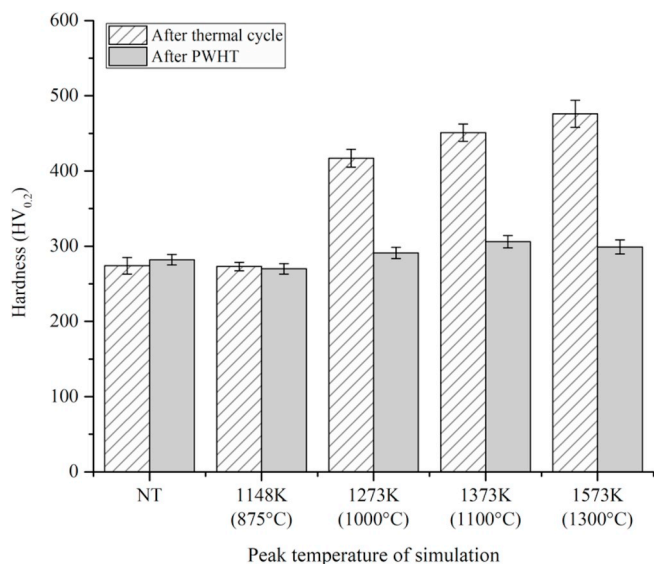


Fig. 9. A graph demonstrating the hardness values measured after weld simulations with various peak temperatures and PWHT.

although the Laves phase particles observed after PWHT are not excessively large, they may grow rapidly upon further exposure to applied stress at a high temperature during subsequent creep exposure. It was thus considered that the condition of PWHT should be further optimised to prevent the presence of Laves phases in the initial state before creep testing.

Based on previous observations of 9% Cr steel welds that have failed in a Type IV manner, creep damage is preferentially accumulated in the

HAZ regions where a refined grain structure is present in combination with an uneven distribution of  $M_{23}C_6$  carbides located on PAGBs [9,20]. Microstructural observations obtained from the current research suggest that a  $T_p$  between  $A_{c_1}$  and  $\sim 1473\text{K} (1200^\circ\text{C})$  results in an incomplete dissolution of  $M_{23}C_6$  carbides and the formation of a refined martensitic substructure. In addition, Laves phase particles are observed to form after the initial PWHT in this steel, which may subsequently coarsen during service. Further work is required to determine the effect of welding on the HAZ structures and subsequent creep performance of cross-weld samples for these grades of MarBN to determine their susceptibility to Type IV failure.

### 5. Conclusions

The thermal cycle applied to IBN1 has been utilised to simulate thermal history in different regions of the HAZ during practical welding processes. Based on microstructural observation, the expected variation in microstructure throughout the HAZ has been accurately determined.

The martensitic microstructure after weld simulation has been shown to vary from an equiaxed grain structure to a duplex grain structure consisting of refined grains on the pre-existing PAG boundaries as a function of peak temperature ( $T_p$ ) experienced during weld simulations.

Dissolution of the pre-existing secondary precipitates from the original parent metal during simulated weld thermal cycles was also observed. The observations also suggest that the un-dissolved  $M_{23}C_6$  carbides hinder the re-austenitisation process and help sustain the duplex grain structure after weld simulation when  $T_p > A_{c_3}$ . The Nb-rich MX carbonitrides are also more stable in the high temperature regions as compared to the V-rich MX precipitate.

During PWHT, both the  $M_{23}C_6$  carbides and the MX carbonitrides were re-precipitated, with the former evenly distributed on the

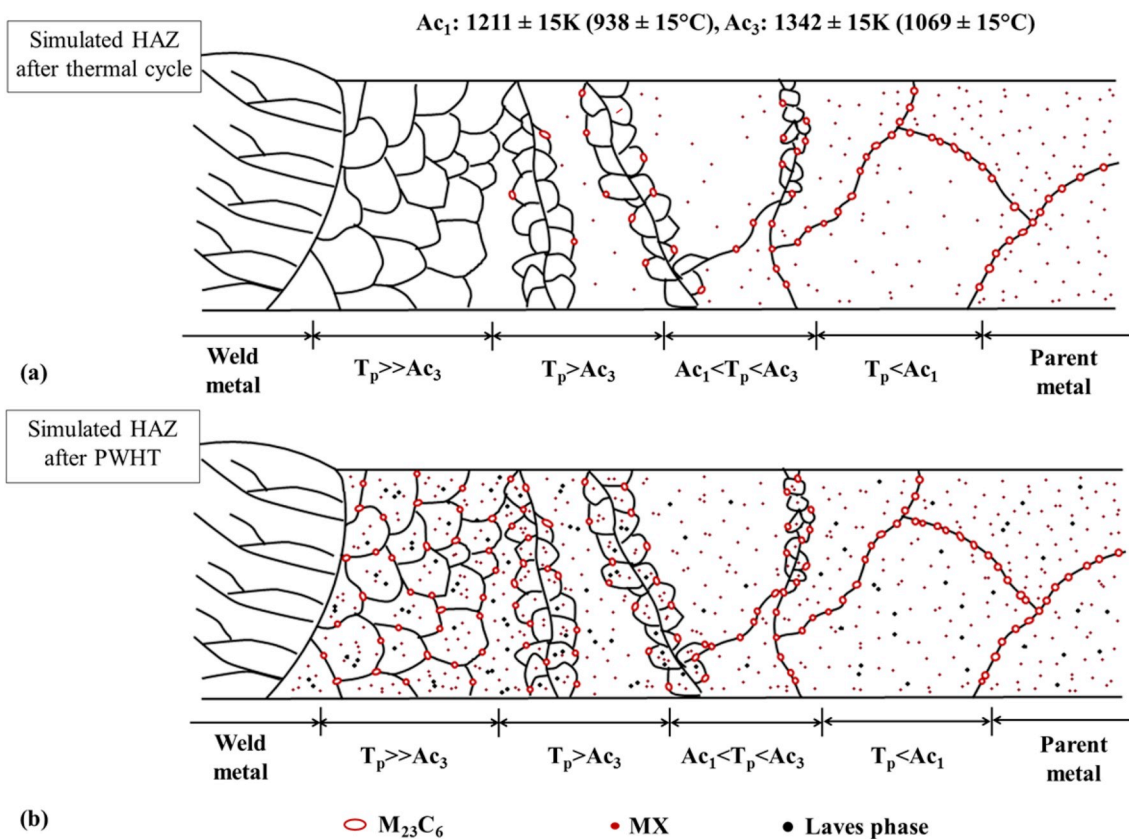


Fig. 10. Schematic diagrams illustrating the microstructural gradient in the HAZ as a function of  $T_p$  after (a) weld simulation and (b) PWHT.

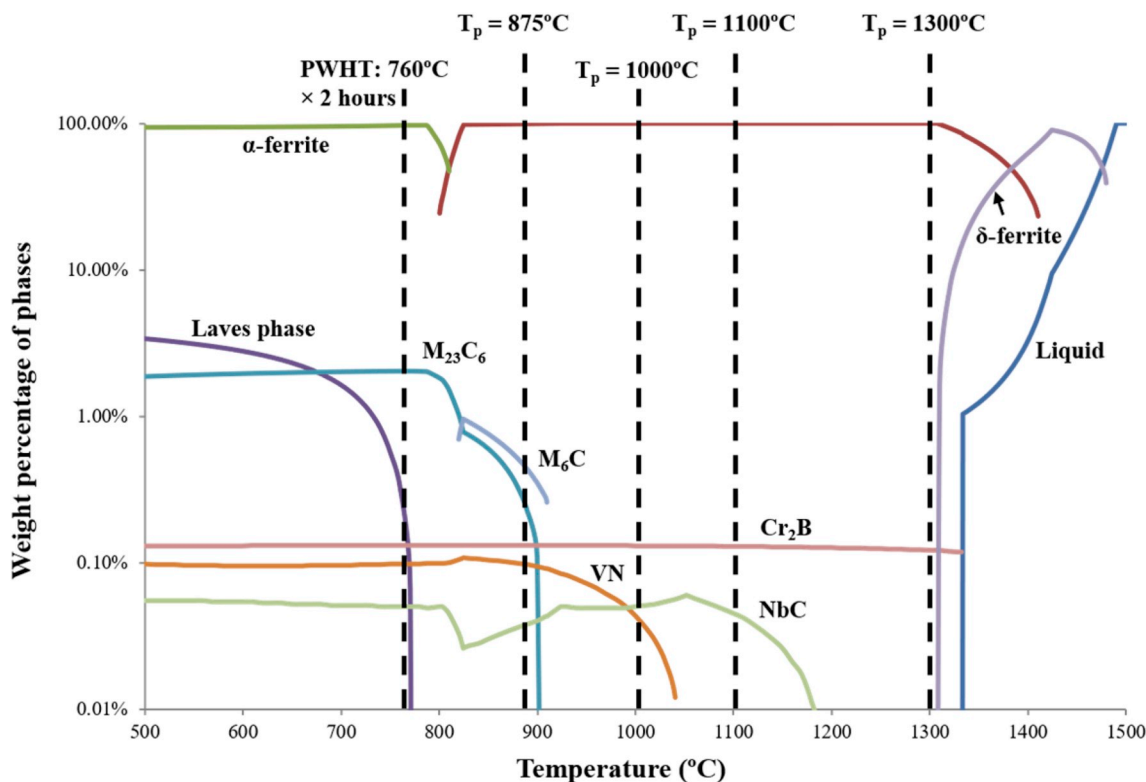


Fig. 11. A graph showing the variation of phase fraction against temperature for the thermodynamic equilibrium state. The calculation was conducted using Thermo-calc software version 2016b with a TCFE 7 database using the chemical composition given in Table 1.

martensitic boundaries. The specimen exposed to a weld simulation with a  $T_p = 1573\text{ K}$  ( $1300\text{ }^\circ\text{C}$ ) demonstrated a higher fraction of  $M_{23}C_6$  carbides within a size range of  $0.1\text{--}0.2\text{ }\mu\text{m}$  for the optimisation of creep resistance. This suggests a higher creep strength in the region close to the weld line than in other parts of the HAZ of a real weld.

Laves phase was also formed to a minor level during PWHT. This may lead to a compromised creep performance of the weld HAZ due to a fast growth of the Laves phase upon creep exposure. It was therefore recommended that the PWHT could be optimised to prevent the formation of Laves phase at the initial stage before creep.

The hardness in the specimens which experienced a higher  $T_p$  during weld simulation decreased more significantly than the specimens exposed to a thermal cycle with a lower  $T_p$ . This suggests a minimised hardness gradient in the HAZ of real welds after PWHT if conducted in an appropriate condition.

### Data availability

The raw/processed data required to reproduce these findings cannot be shared at this time as the data also forms part of an ongoing study.

### Acknowledgments

We would like to acknowledge the support of the Engineering and Physical Research Council (EPSRC) for their support for the project through: Flexible and Efficient Power Plant: Flex-E-Plant (Grant number EP/K021095/1) and EPSRC and Innovate UK through: IMPULSE - Advanced Industrial Manufacture of Next-Generation MARBN Steel for Cleaner Fossil Plant (Grant number: EP/N509942/1). We also thank the following industrial partners for their valuable contributions: GE Power, Doosan Babcock Limited, Centrica plc., EDF Energy (West Burton Power) Limited., Uniper Technologies Limited, Goodwin Steel Castings Limited, NPL Management Limited, R-MC Power Recovery Limited., RWE Generation UK plc., Scottish and Southern Energy (SSE) plc., Siemens Industrial Turbomachinery, TWI Limited, Metrode Products Limited and Wyman-Gordon Limited. We also acknowledge the support of the Loughborough Materials Characterisation Centre (LMCC).

### References

- [1] F. Abe, M. Tabuchi, H. Semba, M. Igarashi, M. Yoshizawa, N. Komar, A. Fujita, Feasibility of MARBN steel for application to thick section boiler components in USC power plant at  $650\text{ }^\circ\text{C}$ , *Adv. Mater. Technol. Foss. Power Plants - Proceedings from 5<sup>th</sup> Int. Conf.*, 2008, pp. 92–106.
- [2] K.G. Abstoss, A. Nitsche, P. Mayr, C. Schlacher, V. González, A. Agüero, Experience with 9Cr3W3CoVnBN steel in terms of welding, creep and oxidation, *Adv. Mater. Technol. Foss. Power Plants - Proceedings from 8th Int. Conf.*, 2016, pp. 990–1001.
- [3] H. Semba, F. Abe, Alloy design and creep strength of advanced 9%Cr USC boiler steels containing high concentration of boron, *Energy Mater.* 1 (2006) 238–244.
- [4] F. Abe, Precipitate design for creep strengthening of 9%Cr tempered martensitic steel for ultra-supercritical power plants, *Sci. Technol. Adv. Mater.* 9 (2008) 13002.
- [5] S.A. David, J.A. Siefert, Z. Feng, Welding and weldability of candidate ferritic alloys for future advanced ultra-supercritical fossil power plants, *Sci. Technol. Weld. Join.* 18 (2013) 631–651.
- [6] C. Schlacher, C. Béal, S. Mitsche, P. Mayr, C. Sommitsch, S. Mitsche, P. Mayr, C. Schlacher, C. Be, Creep and damage investigation of advanced martensitic chromium steel weldments for high temperature applications in thermal power plants, *Sci. Technol. Weld. Join.* 20 (2016) 82–90.
- [7] T. Matsunaga, H. Hongo, M. Tabuchi, R. Sahara, Suppression of grain refinement in heat-affected zone of 9Cr-3W-3Co-VnB steels, *Mater. Sci. Eng. A* 655 (2016) 168–174.
- [8] J.A. Francis, W. Mazur, H. Bhadeshia, Review Type IV cracking in ferritic power plant steels, *Mater. Sci. Technol.* 22 (2006) 1387–1395.
- [9] D.J. Abson, J.S. Rothwell, Review of type IV cracking of weldments in 9–12% Cr creep strength enhanced ferritic steels, *Int. Mater. Rev.* 58 (2013) 437–473.
- [10] H.J. Schuller, L. Hagn, A. Woitscheck, Cracking in the weld region of shaped components in hot steam pipe lines—materials investigations, *Der Maschinenschaden* 47 (1974) 1–13.
- [11] J.S. Lee, K. Maruyama, Mechanism of microstructural deterioration preceding Type IV failure in weldment of mod. 9Cr-1Mo steel, *Met. Mater. Int.* 21 (2015) 639–645.
- [12] M. Tabuchi, T. Watanabe, K. Kubo, M. Matsui, J. Kinugawa, F. Abe, Creep crack growth behavior in the HAZ of weldments of W containing high Cr steel, *Int. J. Press. Vessel. Pip.* 78 (2001) 779–784.
- [13] M.E. Kassner, T.A. Hayes, Creep cavitation in metals, *Int. J. Plast.* 19 (2003) 1715–1748.
- [14] H. Hongo, M. Tabuchi, T. Watanabe, Type IV creep damage behavior in Gr. 91 steel welded joints, *Metall. Mater. Trans. A* 43 (2012) 1163–1173.
- [15] K. Laha, K.S. Chandravathi, P. Parameswaran, K.B.S. Rao, S.L. Mannan, Characterization of microstructures across the heat-affected zone of the modified 9Cr-1Mo weld joint to understand its role in promoting Type IV cracking, *Metall. Mater. Trans. A* 38 (2007) 58–68.
- [16] Y. Wang, R. Kannan, L. Li, Characterization of as-welded microstructure of heat-affected zone in modified 9Cr-1Mo-V-Nb steel weldment, *Mater. Char.* 118 (2016) 225–234.
- [17] K.H. Lee, J.Y. Suh, S.M. Hong, J.Y. Huh, W.S. Jung, Microstructural evolution and creep-rupture life estimation of high-Cr martensitic heat-resistant steels, *Mater. Char.* 106 (2015) 266–272.
- [18] R.W.K. Honeycombe, H.K.D.H. Bhadeshia, *Steels: Microstructure and Properties*, Edward Arnold, London, 1995.
- [19] J.A. Gianetto, J.E.M. Braid, J.T. Bowker, W.R. Tyson, Heat-affected zone toughness of a TMCP steel designed for low-temperature applications, *J. Offshore Mech. Arct. Eng.* 119 (1997) 134–144.
- [20] Y. Liu, S. Tsukamoto, T. Shirane, F. Abe, Formation mechanism of type iv failure in high cr ferritic heat-resistant steel-welded joint, *Metall. Mater. Trans. A* 44 (2013) 4626–4633.
- [21] X. Xu, G.D. West, J.A. Siefert, J.D. Parker, R.C. Thomson, The influence of thermal cycles on the microstructure of Grade 92 steel, *Metall. Mater. Trans. A* 48 (2017) 5396–5414.
- [22] C. Kalk, B. Fournier, B. Françoise, L. Forest, F. Dalle, P.-F. Giroux, I. Tournié, A.-F. Gourgues-Lorenzon, High temperature creep properties and microstructural examinations of P92 welds, 9th Liege Conf. Mater. Adv. Power Eng., 2010, pp. 424–434.
- [23] K. Maruyama, K. Sawada, J. Koike, Strengthening mechanisms of creep resistant tempered martensitic steel, *ISIJ Int.* 41 (2001) 641–653.
- [24] M. Taneike, K. Sawada, F. Abe, Effect of carbon concentration on precipitation behavior of  $M_{23}C_6$  carbides and MX carbonitrides in martensitic 9Cr steel during heat treatment, *Metall. Mater. Trans. A* 35 (2004) 1255–1262.
- [25] X. Xu, G.D. West, J.A. Siefert, J.D. Parker, R.C. Thomson, Microstructural characterization of the heat-affected zones in Grade 92 steel welds: double-pass and multipass welds, *Metall. Mater. Trans. A* 49 (2018) 1211–1230.
- [26] M. Lomozik, Effect of the welding thermal cycles on the structural changes in the heat affected zone and on its properties in joints welded in low-alloy steels, *Weld. Int.* 14 (2000) 845–850.
- [27] T. Vuherer, M. Dunder, L.J. Milovic, M. Zrilic, I. Samardzic, Microstructural investigation of the heat-affected zone of simulated welded joint of P91 steel, *Metalurgija* 52 (2013) 317–320.
- [28] L. Havelka, P. Mohyla, Thermal cycle measurement of P92 welded joints, *Proc. 23rd Int. Conf. Met. Mater.* 2014.
- [29] J.A. Siefert, B.M. Leister, J.N. DuPont, Considerations in development of CCT diagrams for complex ferritic materials, *Mater. Sci. Technol.* 31 (2015) 651–660.
- [30] J.A. Siefert, J.P. Shingledecker, J.D. Parker, Optimization of vickers hardness parameters for micro-and macro-indentation of grade 91 steel, *J. Test. Eval.* 41 (2013) 1–10.
- [31] L. Korcakova, J. Hald, M.A.J. Somers, Quantification of Laves phase particle size in 9CrW steel, *Mater. Char.* 47 (2001) 111–117.
- [32] E. Smith, J. Nutting, Direct carbon replicas from metal surfaces, *Br. J. Appl. Phys.* 7 (1956) 214.
- [33] P. Zhu, L. Li, G. West, R.C. Thomson, The Effect of Stress Relief Heat Treatments on Microstructural Evolution and Mechanical Properties in Grade 91 and 92 Power Plant Steels, (2011), pp. 679–692.
- [34] C.G. Panait, A. Zielińska-Lipiec, T. Koziel, A. Czyska-Filemonowicz, A.F. Gourgues-Lorenzon, W. Bendick, Evolution of dislocation density, size of subgrains and MX-type precipitates in a P91 steel during creep and during thermal ageing at  $600\text{ }^\circ\text{C}$  for more than 100,000 h, *Mater. Sci. Eng. A* 527 (2010) 4062–4069.
- [35] T. Shirane, S. Tsukamoto, K. Tsuzaki, Y. Adachi, T. Hanamura, M. Shimizu, F. Abe, Ferrite to austenite reverse transformation process in B containing 9%Cr heat resistant steel HAZ, *Sci. Technol. Weld. Join.* 14 (2009) 698–707.
- [36] W. Yan, W. Wang, Y.Y. Shan, K. Yang, Microstructural stability of 9–12% Cr ferrite/martensite heat-resistant steels, *Front. Mater. Sci.* 7 (2013) 1–27.
- [37] A. Benaarbia, X. Xu, W. Sun, A.A. Becker, M.A.E. Jepsen, Investigation of short-term creep deformation mechanisms in MarBN steel at elevated temperatures, *Mater. Sci. Eng. A* 734 (2018) 491–505.
- [38] M. Tamura, T. Kumagai, N. Miura, Y. Kondo, K. Shinozuka, H. Esaka, Effect of martensitizing temperature on creep strength of modified 9Cr steel, *Mater. Trans.* 52 (2011) 691–698.
- [39] T. Shrestha, S.F. Alsagabi, I. Charit, G.P. Potirniche, M.V. Glazoff, Effect of heat treatment on microstructure and hardness of Grade 91 steel, *Metals* 5 (2015) 131–149.
- [40] A.H. Yaghi, D.W.J. Tanner, T.H. Hyde, A.A. Becker, W. Sun, Abaqus thermal analysis of the fusion welding of a P92 steel pipe, *SIMULIA Cust. Conf.*, 2011, pp. 622–638.
- [41] A.H. Yaghi, T.H. Hyde, A.A. Becker, W. Sun, Finite element simulation of welding and residual stresses in a P91 steel pipe incorporating solid-state phase transformation and post-weld heat treatment, *J. Strain Anal. Eng. Des.* 43 (2008) 275–293.

- [42] M. Kondo, M. Tabuchi, S. Tsukamoto, F. Yin, F. Abe, Suppressing Type IV failure via modification of heat affected zone microstructures using high boron content in 9Cr heat resistant steel welded joints, *Sci. Technol. Weld. Join.* 11 (2006) 216–223.
- [43] R.C. Maclachlan, J.J. Sanchez-Hanton, R.C. Thomson, The effect of simulated post weld heat treatment temperature overshoot on microstructural evolution in P91 and P92 power plant steels, *Adv. Mater. Technol. Foss. Power Plants - Proc. from 6th Int. Conf. 2011*, pp. 787–799.
- [44] P.J. Ennis, A. Czyrska-Filemonowicz, Recent advances in creep-resistant steels for power plant applications, *Sadhana* 28 (2003) 709–730.
- [45] L. Li, *Microstructural Evolution in 9 wt.% Cr Power Plant Steels*, Loughborough University, 2013.
- [46] F. Abe, H. Araki, T. Noda, The effect of tungsten on dislocation recovery and precipitation behavior of low-activation martensitic 9Cr steels, *Metall. Trans. A* 22 (1991) 2225–2235.
- [47] F. Abe, Effect of fine precipitation and subsequent coarsening of Fe<sub>2</sub>W Laves phase on the creep deformation behavior of tempered martensitic 9Cr-W steels, *Metall. Mater. Trans. A* 36 (2005) 321–332.